Acta Materialia 280 (2024) 120288

Contents lists available at ScienceDirect

Acta Materialia

journal homepage: www.elsevier.com/locate/actamat

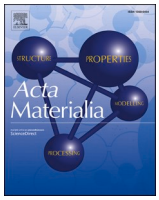

# Effect of carbon segregation at prior austenite grain boundary on hydrogen-related crack propagation behavior in 3Mn-0.2C martensitic steels

Kazuho Okada [a,b,*], Akinobu Shibata [a,c], Yuuji Kimura [a], Masatake Yamaguchi [d,e], Ken-ichi Ebihara [d], Nobuhiro Tsuji [b,c]

[a] Research Center for Structural Materials, National Institute for Materials Science (NIMS), 1-2-1 Sengen, Tsukuba, Ibaraki 305-0047, Japan
[b] Department of Materials Science and Engineering, Kyoto University, Yoshida- honmachi, Sakyo-ku, Kyoto 606-8501, Japan
[c] Elements Strategy Initiative for Structural Materials (ESISM), Kyoto University, Yoshida-honmachi, Sakyo-ku, Kyoto 606-8501, Japan
[d] Center For Computational Science and e-systems, Japan Atomic Energy Agency, Tokai-mura, Ibaraki 319-1195, Japan
[e] Department of Materials Science and Engineering, The University of Tokyo, 7-3-1 Hongo, Bunkyo-ku, Tokyo 113-8656, Japan

ARTICLE INFO

*Keywords:*
Hydrogen embrittlement
Martensitic steel
Crack propagation
Grain-boundary segregation
Intergranular failure

ABSTRACT

The present study aimed at strengthening prior austenite grain boundary (PAGB) cohesive energy using carbon segregation and investigated the effect of carbon segregation at PAGB on the microscopic crack propagation behavior of hydrogen-related intergranular fractures in high-strength martensitic steels. At the low hydrogen content (below 0.2 wt. ppm), the fracture initiation toughness ($J_{IC}$) and tearing modulus ($T_R$), corresponding to crack growth resistance, were significantly improved by carbon segregation. In contrast, $J_{IC}$ and $T_R$ did not change by carbon segregation at the high hydrogen content (above 0.5 wt. ppm). Considering the non-linear relationship between the toughness properties and the PAGB cohesive energy, the experimentally evaluated toughness properties ($J_{IC}$ and $T_R$) and the GB cohesive energy previously calculated by first-principles calculations were semi-quantitatively consistent even at the high hydrogen content. The microstructure observation confirmed that the plastic deformation associated with crack propagation, such as the local ductile fracture of uncracked ligaments and the formation of dislocation cell structures / nano-voids, played an important role in the non-linear relationship between the toughness properties and PAGB cohesive energy.

## 1. Introduction

Since the reduction of automobile weight is required by exhaust gas regulations, it is demanded to commercialize steels with as high strength as possible. However, it is well known that steels become more susceptible to hydrogen embrittlement with increasing their strength level. Hydrogen embrittlement is the phenomenon by which metals and alloys become brittle due to the hydrogen introduction [1–5]. Because the introduction of a certain amount of hydrogen into steels during fabrication and application is inevitable, it has been desired to improve the resistance to hydrogen embrittlement in high-strength steels.

Martensitic steels, which are typical high-strength steels, are highly susceptible to hydrogen embrittlement. Intergranular and quasi-cleavage are the typical fracture modes in the hydrogen-related fracture of martensitic steels. In general, as the hydrogen content increases, fracture mode changes from quasi-cleavage to intergranular which results in more severe embrittlement [6]. A lath martensitic structure consists of several structural units with different size scales, namely, lath, block, packet, and prior austenite grain [7–11]. Although the martensitic structure comprises several types of high-angle boundaries, hydrogen-related intergranular fracture mainly occurs along prior austenite grain boundaries (PAGB) [12–19]. Hydrogen accumulation around PAGB could be the possible reason for preferential intergranular fracture at PAGB [20–23]. It has been revealed that hydrogen reduces the cohesive energy of grain boundaries ($\gamma_{GB}$) in iron using first-principles calculations [2,24,25], molecular statics simulations

* Corresponding author at: Research Center for Structural Materials, National Institute for Materials Science (NIMS), 1-2-1 Sengen, Tsukuba, Ibaraki 305-0047, Japan.
*E-mail addresses:* okada.kazuho@nims.go.jp (K. Okada), shibata.akinobu@nims.go.jp (A. Shibata), kimura.yuuji@nims.go.jp (Y. Kimura), yamaguchi.masatake@jaea.go.jp (M. Yamaguchi), ebihara.kenichi@jaea.go.jp (K.-i. Ebihara), nobuhiro-tsuji@mtl.kyoto-u.ac.jp (N. Tsuji).

https://doi.org/10.1016/j.actamat.2024.120288
Received 23 May 2024; Received in revised form 18 July 2024; Accepted 13 August 2024
Available online 14 August 2024

[26], and molecular dynamics simulations [27]. Recently, Yamaguchi et al. [28] performed first-principles calculations and revealed that carbon segregation at iron GB increased the cohesive energy and effectively suppressed the hydrogen-induced reduction of $\gamma_{GB}$. In addition, we experimentally demonstrated that fracture stress of the hydrogen-charged martensitic steel can be improved by increasing carbon segregation at PAGB [29]. However, the previous study performed uniaxial tensile tests for evaluating hydrogen embrittlement properties, and uniaxial tensile tests are unsuitable for discussing the mechanical response from the fracture mechanics in detail. Because rapid crack propagation in structural materials can lead to serious accidents, it is essential to quantitatively understand the crack propagation behavior from the perspective of fracture mechanics. In general, the fracture process can be divided into three microscopic stages: (i) crack initiation, (ii) start of crack propagation, and (iii) crack propagation leading to final rupture. The mechanical response corresponding to each microscopic fracture stage cannot be evaluated from the fracture stress and elongation obtained from the uniaxial tensile tests. On the other hand, it is well known that a crack-growth resistance curve obtained by elastic-plastic fracture mechanics experiments is useful to evaluate fracture toughness properties corresponding to each microscopic fracture stage. Though crack-growth resistance curves have been applied to ductile fracture in many cases, they were recently also applied to hydrogen-related fracture in martensitic steels [30–32], ferritic steels [33,34], and austenitic steels [35–38]. For example, Shibata et al. [30] obtained crack-growth resistance curves ($J-\Delta a$ resistance curves) of the hydrogen-charged as-quenched martensitic steels by unload compliance tests and evaluated fracture initiation toughness ($J_{IC}$) and tearing modulus ($T_R$). $J_{IC}$ is related to the microscopic fracture stage (ii). $T_R$ represents crack-growth resistance corresponding to the microscopic fracture stage (iii). Furthermore, combining the $J-\Delta a$ resistance curve with microstructure observation allows for comparing fracture behaviors, such as fracture surfaces, crack path, and deformation microstructures, at approximately the same $\Delta a$ between two materials.

The present study utilized the $J-\Delta a$ resistance curve and evaluated the effect of carbon segregation at PAGB on fracture toughness properties under the presence of hydrogen from the perspective of fracture mechanics. In addition, we investigated crack propagation behavior through microstructure observation and discussed the relationship between fracture toughness properties and crack propagation behavior.

## 2. Experimental procedure

An Fe-3Mn-0.2C alloy (Mn: 3.02, C: 0.18, Si: 0.01, P: <0.002, S: 0.001, Al: 0.002, N: 0.002, O: 0.001, and Fe: bal. (wt.%)) was used in the present study. According to the previous study [29], the as-received ingot was heat-treated in two different ways. One is one-step austenitization; the specimen was austenitized at 1100 ℃ for 30 min in a vacuum, ice-brine quenched, and sub-zero cooled in liquid nitrogen. The other is two-step austenitization; after the austenitization (1100 ℃, 30 min), the specimen was held at 790 ℃ (just above $A_3$) for 30 min, followed by ice-brine quenching and sub-zero cooling in liquid nitrogen. The isothermal holding at 790 ℃ aimed at increasing carbon segregation at (prior) austenite grain boundaries. Hereafter, we refer to the specimens with one-step and two-step austenitizations as the "Non-seg specimen" and the "Seg specimen", respectively. As reported previously [29], the size of each structural unit and dislocation density were almost the same between the Non-seg and Seg specimens. On the other hand, the concentration of segregated carbon at PAGB measured by three-dimensional atom probe analysis (3DAP) was 4.58 at.% in the Seg specimen, which was drastically increased from the Non-seg specimen (2.90 at.%). The increase in the concentration of segregated carbon at PAGB does not affect the average carbon concentration at PAG interior (see the supplementary materials). The 0.2 % proof strength ($\sigma_{0.2}$) and tensile strength ($\sigma_B$) of the uncharged Non-seg specimen were 1067 and 1524 MPa, respectively, which were similar to those of the uncharged Seg specimen ($\sigma_{0.2}$: 1032 MPa, $\sigma_B$: 1529 MPa) [29].

After the heat-treatments, pre-cracked compact tension (CT) specimens were prepared (thickness: 12.5 mm, width: 25 mm, and net thickness at the side grooves' root: 10 mm). The pre-cracked CT specimens were cathodically pre-charged with hydrogen in an aqueous solution of 3 % NaCl + 3 g $L^{-1}$ $NH_4SCN$ for 72 h at room temperature. We have confirmed that a charging period of 72 h was enough for the homogenous hydrogen distribution inside the present specimen geometries because the diffusible hydrogen content ($H_D$) saturated before 72 h and did not increase with charging periods longer than 72 h [30]. To obtain the specimens with different hydrogen contents, the current density of the hydrogen charging was changed from 0.005 to 2.0 A $m^{-2}$. The $H_D$ was measured by thermal desorption spectroscopy (TDS) using a quadru-pole mass (Q-mass) spectrometer (R-DEC: HTDS-002) at a heating rate of 100 ℃ $h^{-1}$. For the TDS measurements, specimens with a dimension of ~12.5 × 15 × 15 $mm^3$ were used. The cumulative hydrogen content desorbed below 500 ℃ was regarded as $H_D$. The interval between the completion of hydrogen pre-charging and the start of TDS measurement was always 40 min, including contingency time added to the minimum required operation time of 25 min. We have confirmed that the difference in the $H_D$ between the intervals of 25 and 40 min was negligibly small at a current density of 1.0 A $m^{-2}$ (Non-seg specimen).

After the pre-chargings, unloading compliance tests based on the single specimen test method of ASTM E1820 were performed under concurrent hydrogen-charging conditions at the same current densities as the pre-chargings. The concurrent chargings aimed at preventing the desorption of homogeneously distributed hydrogen after the pre-chargings. $J-\Delta a$ resistance curves were obtained from the results of unload compliance tests according to ASTM E1820. Crack mouth opening displacement (CMOD) was measured using a clip gauge. The elastic compliance at a certain CMOD was determined by unload/reload sequences repeated three times. All of the unload/reload sequences were conducted for a displacement interval of 0.0200 and 0.0070 mm in the uncharged and hydrogen-charged specimens, respectively. $\Delta a$, crack extension, can be obtained from the change in elastic compliance in accordance with ASTM E1820, and $J$ is the sum of the elastic component and the plastic component. The elastic component was computed from linear elastic fracture mechanics, while the plastic component was incrementally computed using the plastic area under the load – CMOD curves. The unloading compliance tests were carried out under displacement control at the CMOD rate of 1.0 × $10^{-4}$ mm $s^{-1}$. The unload compliance test for each charging condition was repeated three times to ensure reproducibility. From the $J-\Delta a$ resistance curves, $J_{IC}$ and $T_R$ were evaluated. The $J_{IC}$ is defined as the $J$-integral value at the intersection of the $J-\Delta a$ resistance curve and 0.2 mm offset line whose slope is $\sigma_{0.2}+\sigma_B$. We confirmed that all of the tested specimens satisfied the specimen size criteria for obtaining valid plane-strain $J_{IC}$ according to ASTM E1820. The $T_R$ is defined as the following equation;

$$T_R = \frac{E}{{\sigma_{0.2}}^2}\frac{dJ}{d\Delta a} \quad (1)$$

where $E$ is Young's modulus (= 200 GPa), and $dJ/d\Delta a$ is the average slope of the $J-\Delta a$ resistance curve after the intersection with the 0.2 mm offset line and before the intersection with the 1.5 mm offset line. We used $\sigma_{0.2}$ and $\sigma_B$ of the uncharged specimens obtained from the uniaxial tensile tests because almost all the hydrogen-charged specimens fractured within the elastic strain regime [29].

The microstructures, fracture surfaces, and crack morphologies were characterized using optical microscopy, scanning electron microscopy (SEM, JEOL: JSM-7800F), and electron backscattering diffraction in SEM (EBSD, JEOL: JSM-7100F). The EBSD measurement (step size: 0.2 μm, acceleration voltage: 15 kV) and analysis were performed with the TSL OIM Data Collection program and the TSL OIM Analysis program, respectively. Using a focused ion beam (FIB, FEI: Quanta 3D 200i), thin

foils were lifted out from the hydrogen-related intergranular fracture surface. The lifted-out samples were observed by scanning transmission electron microscopy (STEM, JEOL: JEM-2100F) at an acceleration voltage of 200 kV. According to the K-S orientation relationships [9,10], the number of each martensite variant was determined by orientation analysis using Kikuchi diffraction patterns.

## 3. Results

Fig. 1 shows the optical microscopy images of microstructures in the Non-seg and Seg specimens. Both specimens show fully lath martensitic microstructures and the average PAG sizes were 183 and 187 μm in the Non-seg (Fig. 1(a)) and Seg (Fig. 1(b)) specimens, respectively [29]. Fig. 2 presents the $H_D$ of specimens after the hydrogen pre-chargings at different current densities measured by TDS. The $H_D$ was almost the same value between the Non-seg and Seg specimens at an identical current density and increased with increasing current density. Both the uncharged Non-seg and Seg specimens did not contain diffusible hydrogen ($H_D$ = 0.0 wt. ppm). It should be noted that all the following results were summarized by current density, not by $H_D$. This is because the fracture toughness properties obtained under concurrent hydrogen charging conditions were different between 0.005 and 0.1 A m$^{-2}$ (Fig. 3) though $H_D$ after the pre-chargings were similar values between these current densities (~0.2 wt. ppm) (Fig. 2).

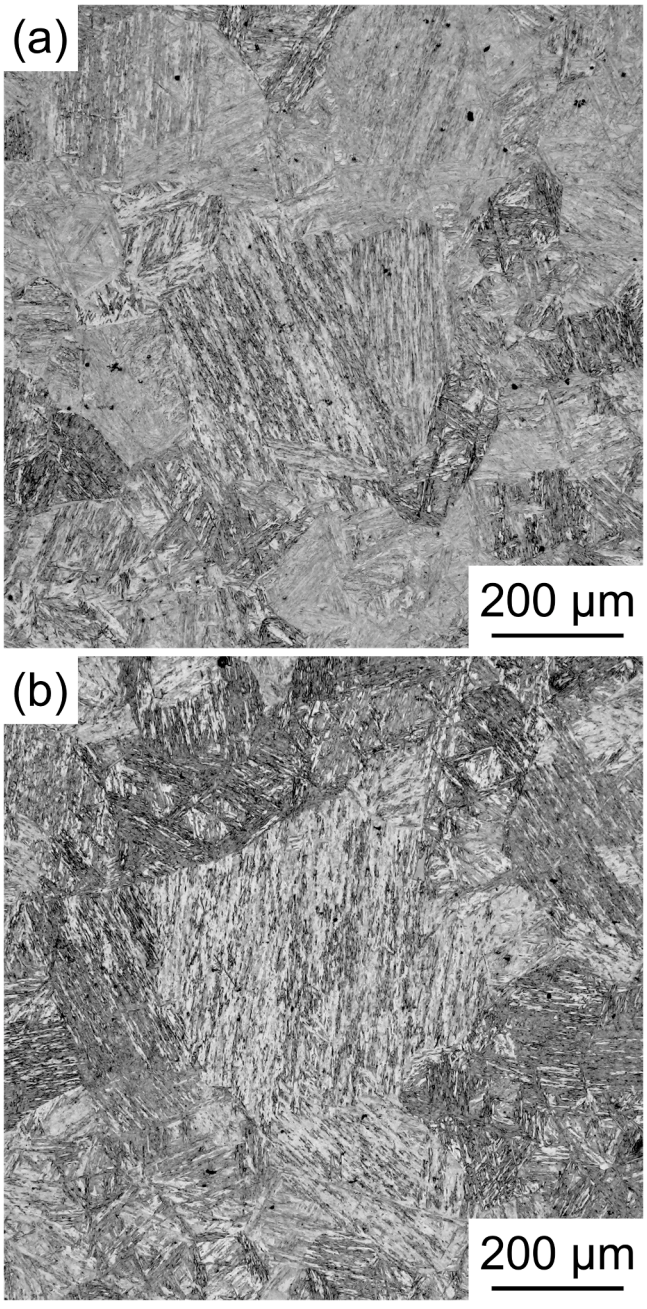


**Fig. 1.** Optical microscopy images of the lath martensitic microstructures after the heat treatments ((a) Non-seg specimen and (b) Seg specimen).

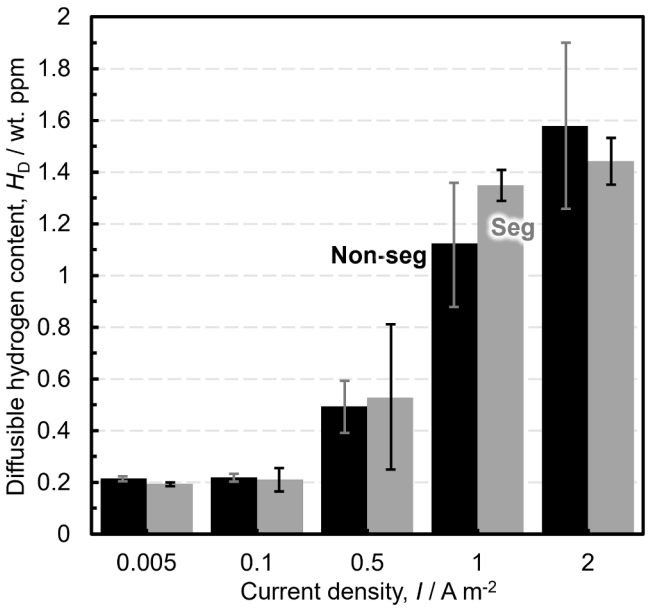


**Fig. 2.** Relationship between the diffusible hydrogen content ($H_D$) and the current density in the cathodic hydrogen charging.

Fig. 3(a, b) show the load – CMOD curves with different current densities in the Non-seg and Seg specimens, respectively. The slope of unload/reload sequences decreased with increasing CMOD, which means $\Delta a$ increased. Fig. 3(c) presents the obtained $J$ – $\Delta a$ resistance curves, and Fig. 3(d) is the enlarged view of the hydrogen-charged specimens in (c). We can find that the $J$-integral values at an identical $\Delta a$ decreased with increasing current density both in the Non-seg and Seg specimens. However, even at the highest current density (light blue, 2.0 A m$^{-2}$, $H_D$ ~ 1.5 wt. ppm), positive slopes of the $J$ – $\Delta a$ resistance curves are confirmed after the start of crack propagation both in the Non-seg and Seg specimens. As we reported previously [30,39], the results indicate that the hydrogen-related fracture is not a completely unstable brittle fracture, but involves a kind of stable crack propagation stage. This is because positive $dJ/d\Delta a$ requires the supply of strain energy by the external load for further crack propagation [40]. The $J_{IC}$ and $T_R$ evaluated using the $J$ – $\Delta a$ resistance curves (Fig. 3(c, d)) are summarized in Fig. 3(e, f), respectively. In the uncharged specimens, the $J_{IC}$ was higher in the Seg specimen (red), whereas the $T_R$ was higher in the Non-seg specimen (black). Both the $J_{IC}$ and $T_R$ of the hydrogen-charged specimens were significantly reduced from the uncharged specimens even at the lowest current density (0.005 A m$^{-2}$). This indicates that a small amount of hydrogen can promote crack propagation. Further increase of the current density led to the gradual decreases of the $J_{IC}$ and $T_R$. In addition, below 0.1 A m$^{-2}$ ($H_D$ ~ 0.2 wt. ppm), the $J_{IC}$ and $T_R$ were much higher in the Seg specimen than those in the Non-seg specimen, demonstrating that carbon segregation at PAGB suppressed the promotion of crack propagation by hydrogen. However, above 0.5 A m$^{-2}$ ($H_D$ ~ 0.5 wt. ppm), the $J_{IC}$ and $T_R$ were almost the same between the Non-seg and Seg specimens.

Fig. 4 shows the SEM images of the fracture surfaces after the unload compliance tests; the uncharged Non-seg specimen (Fig. 4(a-1–3)), the

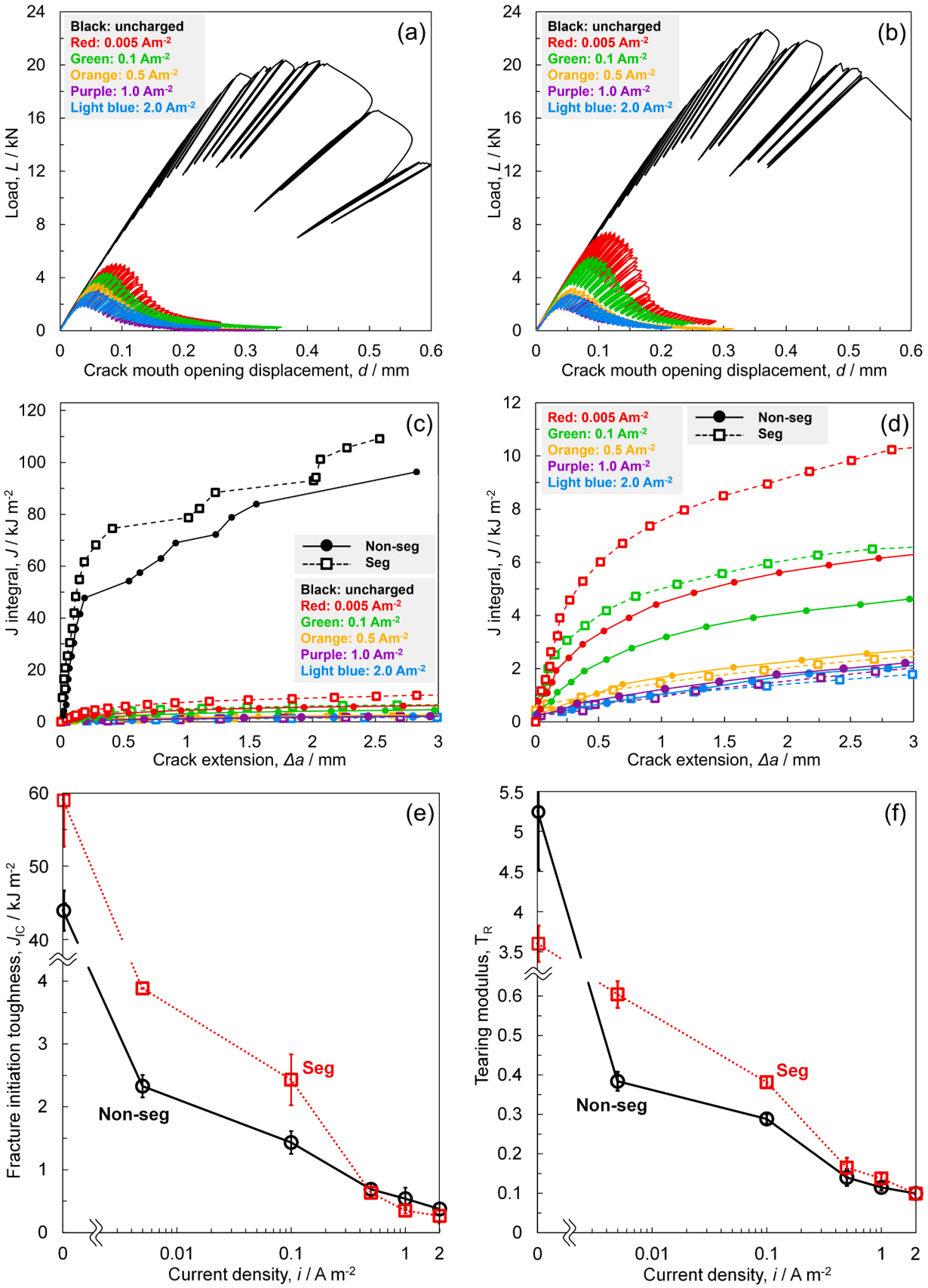


**Fig. 3.** Load – crack mouth opening displacement (CMOD) curves of the (a) Non-seg specimens and (b) Seg specimens at various current densities. Crack growth resistance curves ($J$ – $\Delta a$ resistance curves) of (c) all the specimens and (d) only the hydrogen-charged specimens. Changes in (e) fracture initiation toughness ($J_{IC}$) and (f) tearing modulus ($T_R$) with current density in the Non-seg specimens (black, circle) and the Seg specimens (red, square).

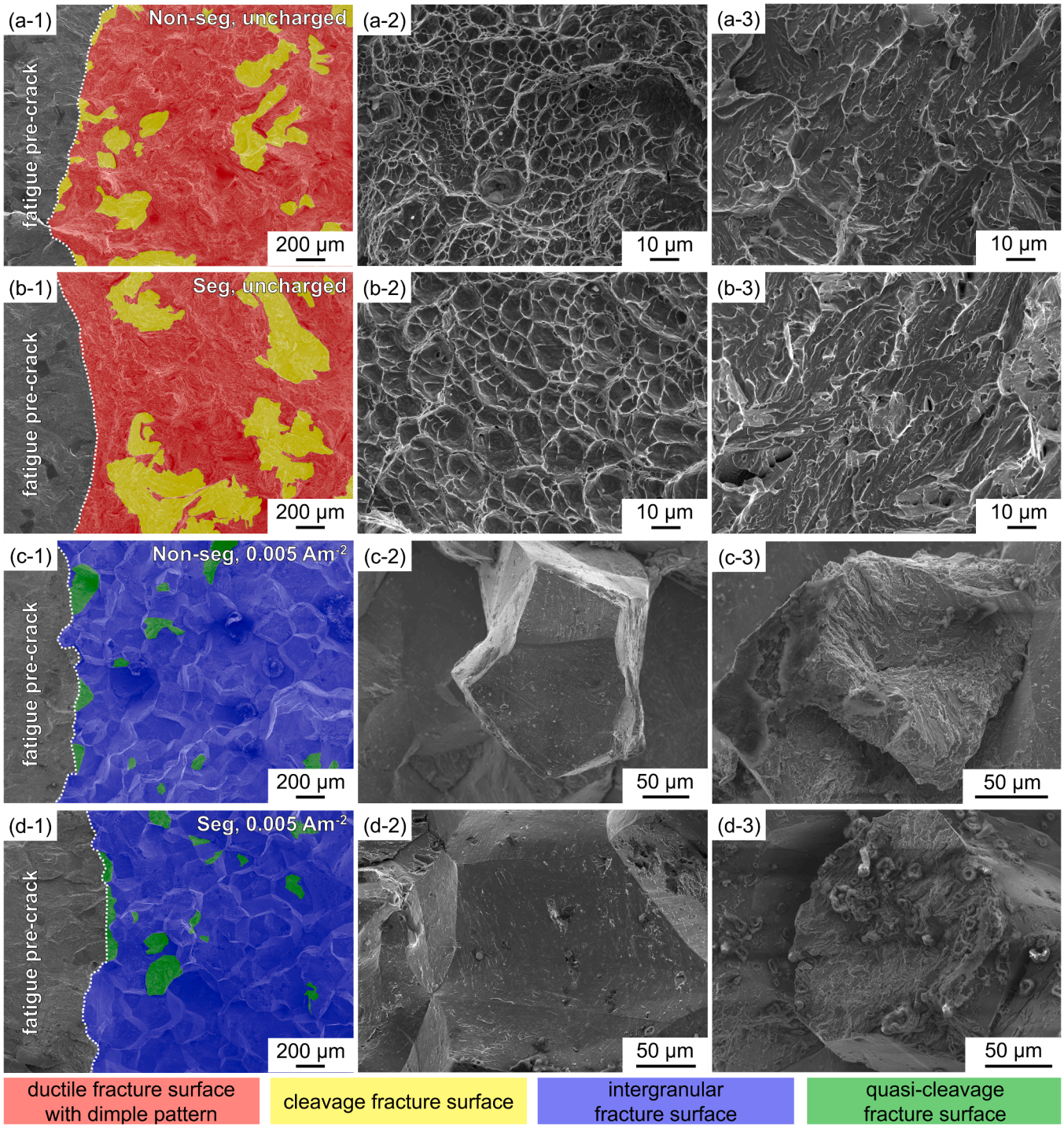


**Fig. 4.** SEM images showing the fracture surfaces after the unloading compliance tests; (a) the uncharged Non-seg specimen, (b) the uncharged Seg specimen, (c) the hydrogen-charged Non-seg specimen (0.005 A $m^{-2}$), and (d) the hydrogen-charged Seg specimen (0.005 A $m^{-2}$). (a–d-1) Low-magnification images in which the regions of ductile fracture surfaces with dimple patterns, cleavage fracture surfaces, intergranular fracture surfaces, and quasi-cleavage fracture surfaces are indicated by red, yellow, blue, and green, respectively. (a-2, 3), (b-2, 3), (c-2, 3), and (d-2, 3) are the high-magnification images of typical fracture surfaces in (a-1), (b-1), (c-1), and (d-1), respectively.

uncharged Seg specimen (Fig. 4(b-1–3)), the hydrogen-charged Non-seg specimen (0.005 A $m^{-2}$, Fig. 4(c-1–3)), and the hydrogen-charged Seg specimen (0.005 A $m^{-2}$, Fig. 4(d-1–3)). Fig. 4(a~d-1) are the low-magnification images in which the regions of ductile fracture surfaces with dimple patterns, cleavage fracture surfaces, intergranular fracture surfaces, and quasi-cleavage fracture surfaces are indicated by red, yellow, blue, and green, respectively. Fig. 4(a~d-2, 3) are the high-magnification images of typical fracture surfaces. In this study, the fracture surface around the mid-thickness section of each specimen, with $\Delta a$ below ~2 mm, was observed because the maximum $\Delta a$ used for calculating the toughness properties, that is, the intersection of the $J$ – $\Delta a$ resistance curve and the 1.5 mm offset line, was always smaller than 2 mm. Because cleavage and quasi-cleavage surfaces are characterized by river patterns and serrated markings, respectively, we can distinguish them from a morphological perspective [13,14,41]. In the uncharged specimens, ductile fracture surfaces with dimple patterns (Fig. 4(a-2)

and (b-2)) and cleavage fracture surfaces (Fig. 4(a-3) and (b-3)) were observed. The fraction of ductile fracture surface was higher in the Non-seg specimen (84.7 %) than in the Seg specimen (71.5 %), which is consistent with the higher $T_R$ in the uncharged Non-seg specimen. However, we could not find any cleavage fracture surface adjacent to the tip of fatigue pre-crack in the Seg specimen (Fig. 4(b-1)), while it was observed in the Non-seg specimen (Fig. 4(a-1)). This would lead to the higher $J_{IC}$ in the Seg specimen because $J_{IC}$ can be correlated to the resistance against the start of crack propagation. In the hydrogen-charged specimens, intergranular fracture surfaces (Fig. 4 (c-2) and (d-2)) and quasi-cleavage fracture surfaces (Fig. 4(c-3) and (d-3)) were observed, and ductile fracture surface with dimple pattern and cleavage fracture surface were not observed. Therefore, we conclude that the change in fracture mode led to the significant decreases in the $J_{IC}$ and $T_R$ by the presence of hydrogen. We confirmed that the fracture surfaces were also covered by intergranular surfaces and quasi-cleavage surfaces in the hydrogen-charged specimens at current densities other than 0.005 A $m^{-2}$ (Fig. S1). The fracture surfaces within approximately 2 mm square areas were observed in three specimens for each test condition, and the fractions of intergranular fracture surfaces are summarized as a function of current density in Fig. 5. Intergranular fracture was the dominant fracture mode and the fraction of intergranular fracture surface was almost the same between the Non-seg and Seg specimens at each current density. For example, the fractions of intergranular fracture surfaces were 94.8 % and 94.3 % in the Non-seg and Seg specimens, respectively, at a current density of 0.005 A $m^{-2}$. This indicates that the improvement of the $J_{IC}$ and $T_R$ in the Seg specimen, particularly below 0.1 A $m^{-2}$, was not due to the change in fracture mode.

To investigate the microscopic crack propagation behavior, the unloading compliance tests at a current density of 0.005 A $m^{-2}$ were stopped at $\Delta a \sim 0.8$ mm, and the mid-thickness sections of the tested Non-seg and Seg specimens were observed. Fig. 6 shows (a) an SEM image, (b) the corresponding EBSD orientation map at a region around the main crack in the Non-seg specimen, and (c–e) SEM-BSE images whose observed areas are the white rectangles indicated in (a). The cracks mainly propagated along the PAGB indicated by the white broken lines in Fig. 6(b). This is consistent with the high fraction (94.8 %) of the intergranular fracture surface. As indicated by the yellow arrows in Fig. 6(a), large uncracked ligaments with ~100 μm length were observed. In addition, small uncracked ligaments with 0.5–3 μm length were formed near the crack-tip regions (red arrows, Fig. 6(c)). The results demonstrate that the hydrogen-related crack discontinuously propagated both in macroscopic and microscopic scales. As shown in Fig. 6(d), dislocation cell structures were formed in front of the arrested intergranular crack tip which started to deviate from the PAGB. It was also found that the arrested intergranular crack started to propagate in a transgranular manner, coalescing nano-voids (green arrows, Fig. 6(e)). The macroscopically / microscopically discontinuous crack propagation along PAGB was also observed in the Seg specimen as shown in Fig. 7 (a–c): (a) SEM image, (b) EBSD orientation map corresponding to (a) at a region around the main crack in the Seg specimen, and (c) SEM-BSE image whose observed area is the white rectangle indicated in (a). Fig. 7(d) shows SEM-BSE images around the tip of the arrested crack whose observed area is the white rectangle indicated in (a). Fig. 7(e) is the enlarged view corresponding to the yellow rectangle in (d). It is clear that the arrested intergranular crack started to deviate from the PAGB, forming dislocation cell structures and nano-voids (indicated by green arrows) within a lath in front of the crack tip. As explained above, the hydrogen-related crack propagation behaviors, such as the macroscopical / microscopical discontinuity and the formation of dislocation cell structures / nano-voids within a lath, were mostly the same between the Non-seg and Seg specimens. The total lengths of observed cracks ($L_{crack}$) in Figs. 6(a) and 7(a), including the crack meandering and the secondary cracks, against the $\Delta a$ were evaluated. Here, the $\Delta a$, crack extension length, is the crack length projected in the section perpendicular to the load line direction (TD section). We found that the $L_{crack}/\Delta a$ value was 1.92 in the Non-seg specimen, which was larger than that in the Seg specimen ($L_{crack}/\Delta a = 1.34$). This means that the degree of crack meandering was larger and the secondary crack length was longer in the Non-seg specimen.

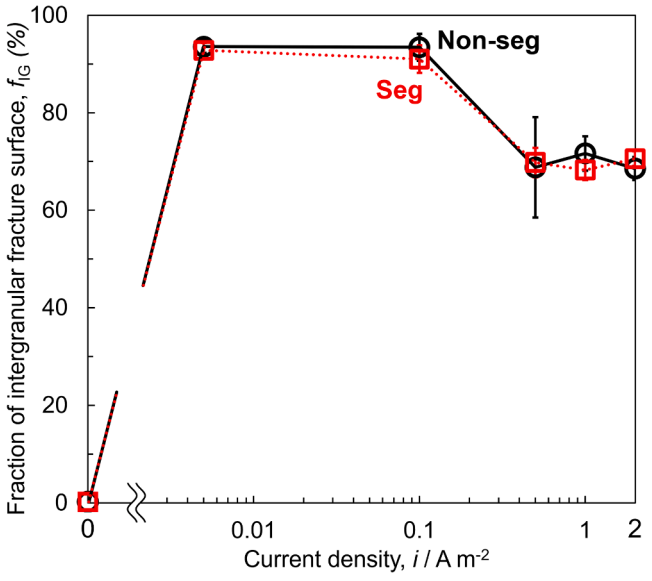


**Fig. 5.** Relationship between the fraction of intergranular fracture surface and current density in the Non-seg specimens (black, circle) and the Seg specimens (red, square).

## 4. Discussion

As shown in Fig. 3(e, f), the $J_{IC}$ and $T_R$ were reduced to one-tenth by the presence of hydrogen even at the lowest current density (0.005 A $m^{-2}$) both in the Non-seg and Seg specimens. These reductions originated from the change in fracture mode, i.e., from a ductile manner in the uncharged specimens (Fig. 4(a, b)) to an intergranular manner in the hydrogen-charged specimens (Fig. 4(c, d)). This would be due to the reduction of the PAGB cohesive energy ($\gamma_{PAGB}$) by hydrogen [2,24–27].

Even though the hydrogen-related crack propagated mainly in an intergranular manner, the macroscopical / microscopical discontinuity (Fig. 6(a–c) and 7(a–c)) and the formation of dislocation cell structure / nano-voids within a lath (Figs. 6(d, e) and 7(d, e)) were observed both in the Non-seg and Seg specimens. Fig. 8 shows (a) an SEM image of the intergranular fracture surface in the Non-seg specimen hydrogen-charged at 0.005 A $m^{-2}$, (b) an enlarged view of the red rectangle in (a), (c) an STEM image of the microstructure beneath the white solid line in (b), and (d, e) enlarged views of the red rectangles in (c). The hydrogen-related intergranular fracture surface was accompanied by stripe patterns (Fig. 8(a)). As shown in Fig. 8(c), these stripe patterns were formed along the lath boundaries, block boundaries (yellow dotted lines), and packet boundaries (yellow solid lines), which were characterized by orientation analysis using Kikuchi diffraction patterns. In addition, some patterns corresponded with the protuberances that could be formed by plastic deformation (Fig. 8(d, e)). The result suggests that the stripe patterns are the traces of local ductile fracture of small uncracked ligaments (Figs. 6(c) and 7(c)), which are evidence of plastic deformation. This is consistent with the previous reports [15,42] that the hydrogen-related intergranular cracks were arrested at the PAGB segments with small misorientation, forming small uncracked ligaments. It is presumed that the misorientation of PAGB changed across the substructure boundaries and the local ductile fracture at small uncracked ligaments corresponded to the protuberances formed on the intergranular fracture surface. The formation of dislocation cell

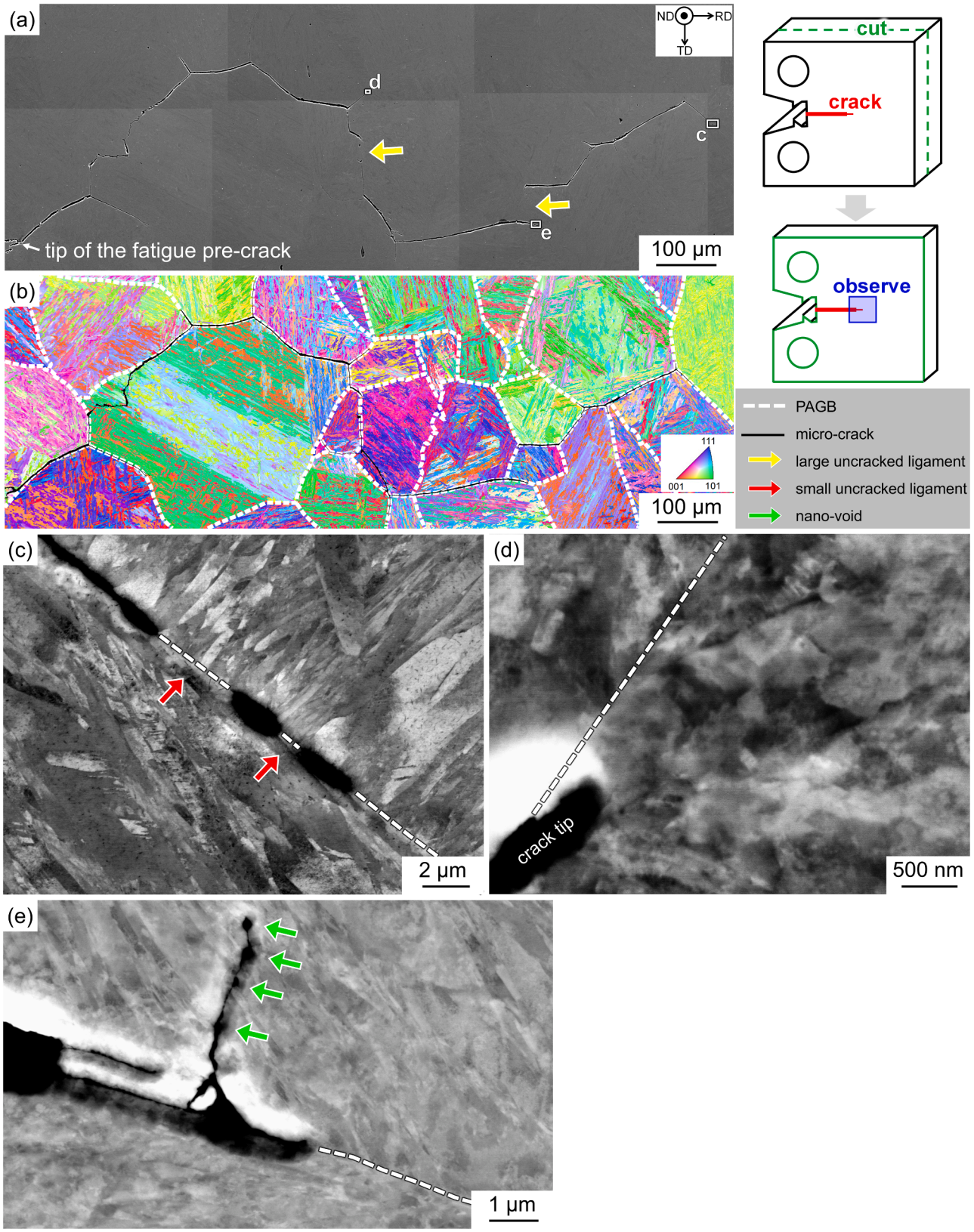


**Fig. 6.** (a) SEM image and (b) corresponding EBSD orientation map at a region around the main crack in the hydrogen-charged Non-seg specimen (0.005 A $m^{-2}$) after the unloading compliance test stopped at $\Delta a \sim 0.8$ mm. (c–e) SEM-BSE images whose observed areas are the white rectangles indicated in (a). The white broken lines, black lines, yellow arrows, red arrows, and green arrows indicate the positions of prior austenite grain boundaries (PAGB), micro-cracks, large uncracked ligaments, small uncracked ligaments, and nano-voids, respectively.

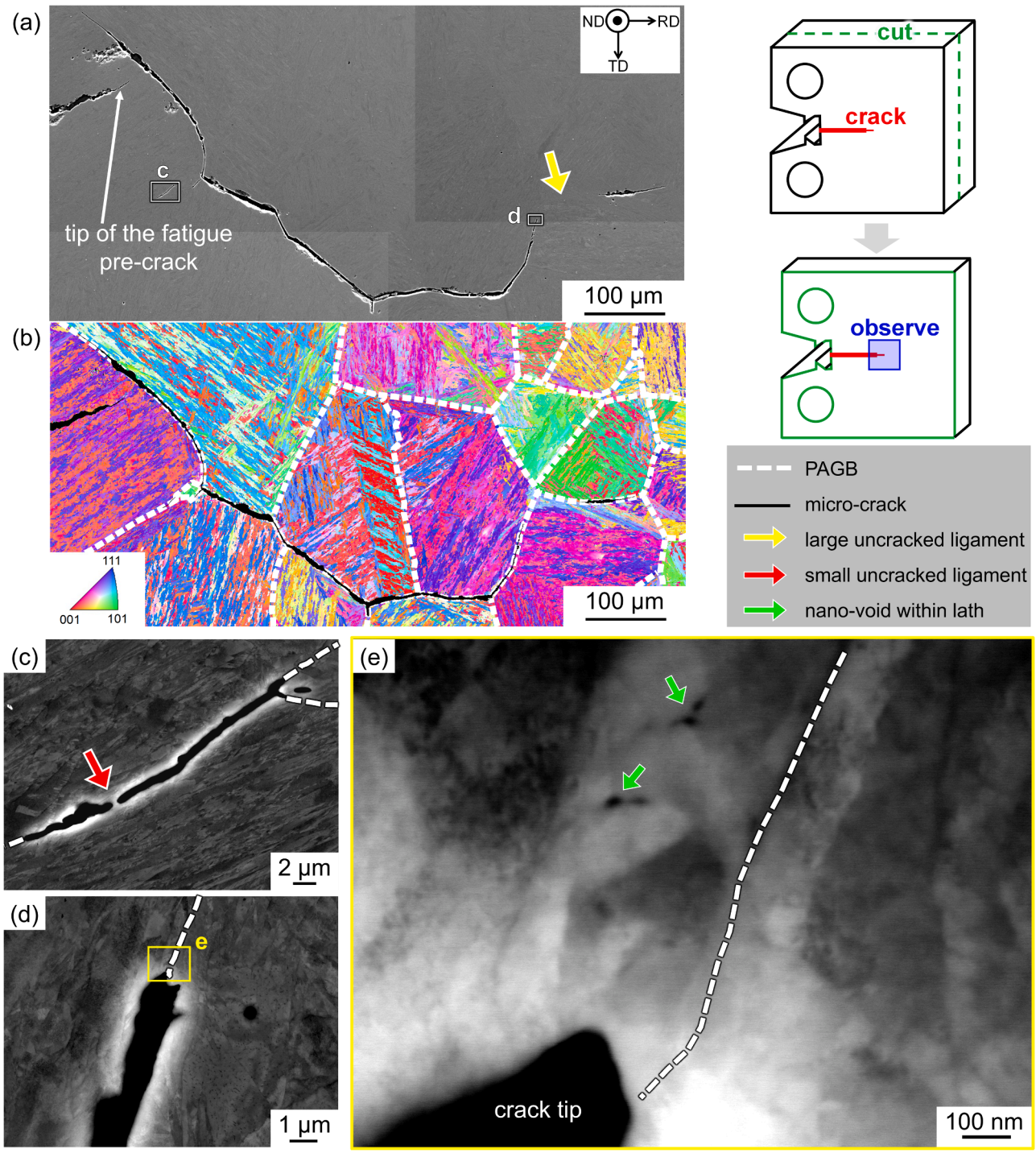


**Fig. 7.** (a) SEM image and (b) corresponding EBSD orientation map at a region around the main crack in the hydrogen-charged Seg specimen (0.005 A $m^{-2}$) after the unloading compliance test stopped at $\Delta a \sim 0.8$ mm. (c, d) SEM-BSE images whose observed areas are the white rectangles indicated in (a). (e) is the enlarged view of the yellow rectangle in (d). The white broken lines, black lines, yellow arrow, red arrows, and green arrows indicate the positions of prior austenite grain boundaries (PAGB), micro-cracks, a large uncracked ligament, small uncracked ligaments, and nano-voids within a lath, respectively.

structures and nano-voids within a lath (Figs. 6(d, e) and 7(d, e)) suggests that the arrested intergranular crack started to propagate in a quasi-cleavage manner. Lynch [1,43], Neeraj et al. [44], Okada et al. [45–47], and Doshida et al. [48] reported that the coalescence of nano-voids led to the hydrogen-related quasi-cleavage fracture. The plastic deformation-mediated mechanisms of the hydrogen-related quasi-cleavage fracture have been also reported in many previous works [49–51]. Therefore, the contribution of these plastic deformations would be one of the origin for stable crack propagation which corresponds to the positive slopes of the $J - \Delta a$ resistance curves in Fig. 3 (c, d).

In the hydrogen-charged specimens at current densities below 0.1 A $m^{-2}$ ($H_D \sim 0.2$ wt. ppm), the $J_{IC}$ and $T_R$ were much higher in the Seg specimen than those in the Non-seg specimen, demonstrating that carbon segregation at PAGB mitigated the crack propagation by hydrogen (Fig. 3(e, f)). Considering the nearly same fraction of intergranular fracture surface between the Non-seg and Seg specimens at an identical current density (Fig. 5), the improvement in the toughness properties

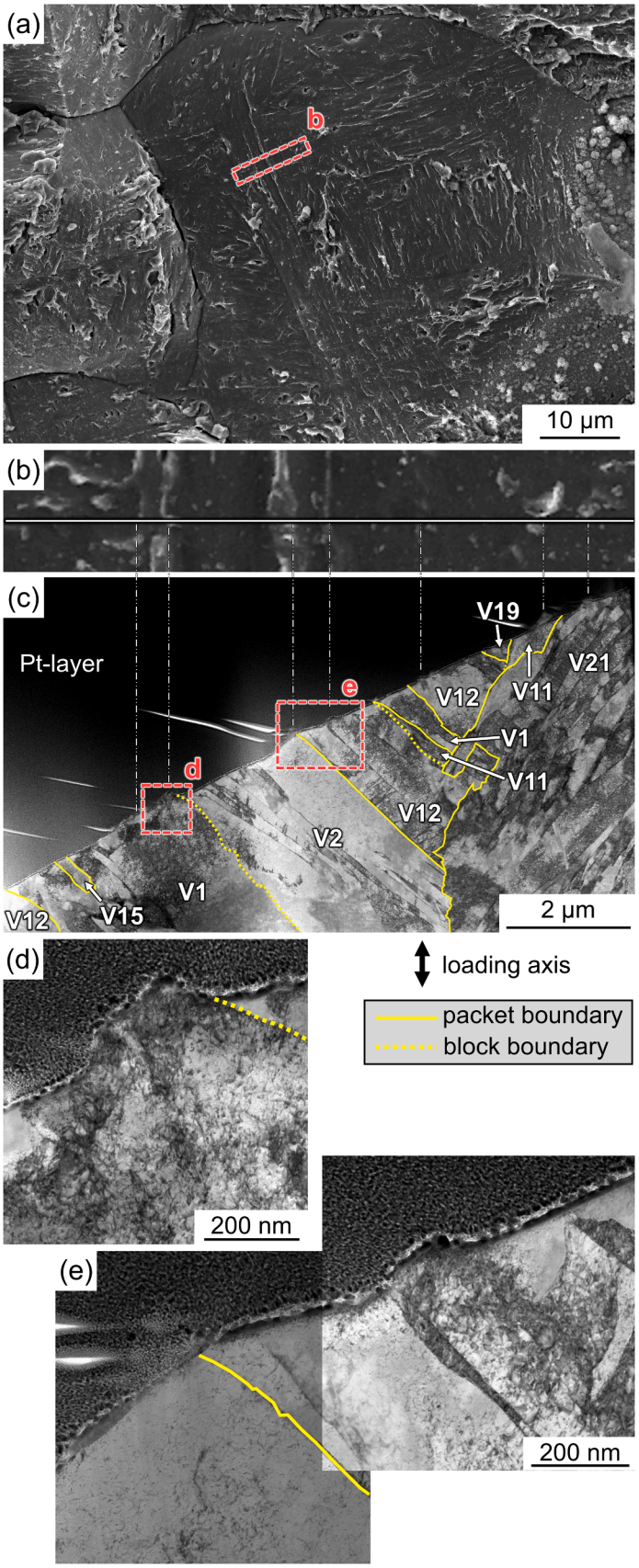


**Fig. 8.** (a) SEM image of the intergranular fracture surface in the Non-seg specimen hydrogen charged at 0.005 A $m^{-2}$, (b) an enlarged view of the red rectangle in (a), (c) STEM image of the microstructure beneath the white solid line in (b), and (d, e) enlarged views of the red rectangles in (c). Yellow dotted lines and yellow solid lines in (c–e) indicate the potions of block boundaries and packet boundaries, respectively.

would originate from the intrinsically increased energy necessary for intergranular fracture per unit area, rather than the change in fracture mode. The first-principles calculations reported by Yamaguchi and Kameda [24,28] indicated that carbon segregation at GB in iron has two effects on the hydrogen-related intergranular cracking. Firstly, the segregated carbon atoms reduce the occupancy of hydrogen atoms at the GB by site competition. Secondly, the segregated carbon atoms increase $\gamma_{GB}$. They proposed that these effects of segregated carbon resulted in the suppression of the reduction of $\gamma_{GB}$ by hydrogen. It has been reported that hydrogen accumulated around PAGB during tensile deformation, and the accumulated hydrogen induced intergranular cracking [22,23]. According to the previous first-principles calculations [24,28], we conclude that the hydrogen accumulation around the PAGB was suppressed by site competition, and the $\gamma_{PAGB}$ was increased by carbon segregation in the Seg specimen. As a result, resistance against the hydrogen-related intergranular fracture (that is, $J_{IC}$ and $T_R$) was improved.

On the other hand, above 0.5 A $m^{-2}$ ($H_D \sim 0.5$ wt. ppm), the $J_{IC}$ and $T_R$ did not change by carbon segregation (Fig. 3(e, f)). This result can appear to be not consistent with the previous results of first-principles calculations [28] that the $\gamma_{GB}$ of iron was increased by carbon segregation even at the extremely high $H_D$ ($\sim 10^5$ atm. ppm, $1.8 \times 10^3$ wt. ppm). However, the hydrogen embrittlement properties experimentally evaluated in the present study are consistent with those evaluated by first-principles calculations, when we consider the non-linear relationship between the $\gamma_{GB}$ and microscopic fracture toughness around an intergranular crack path ($k_{IC}$). An intergranular crack propagates when the strain energy release rate reaches the microscopic fracture work ($w_f$), which is defined by $k_{IC}$, $E$, and Poisson's ratio ($\nu$) [52–54]. The energy criterion for intergranular crack propagation is expressed by the following equation [55,56].

$$(1-\nu^2){k_{IC}}^2/E = w_f = \gamma_{GB} + \gamma_p \quad (2)$$

The $w_f$ is the sum of the $\gamma_{GB}$ and the plastic work ($\gamma_p$) that is much larger than the $\gamma_{GB}$. Yamaguchi et al. [57,58] performed the combined analysis with the density functional theory (DFT) calculations of Σ3(111) GB in iron and the fracture mechanics experiments using Ni-Cr steels, which were mainly fractured in an intergranular manner, and found that the $\gamma_p$ is the function of the $\gamma_{GB}$. As a result, they proposed the non-linear relationship between the $\gamma_{GB}$ and macroscopic fracture toughness ($K_{IC}$). To quantitatively compare the present experimental study and the above DFT results, it is necessary to understand the density of segregated carbon within the PAGB layer ($X_{PAGB}$) in the Non-seg and Seg specimens. As shown in the schematic illustrations (Fig. 9(a)), the concentration profiles of segregated carbon atoms at PAGB measured by 3DAP had a spread of about 10 nm, which is due to the artifact of 3DAP measurement. The detailed concentration profiles can be found in our previous study [29]. Using Auger electron spectroscopy, Seah [59] measured the concentration of segregated interstitial elements at GB in iron and

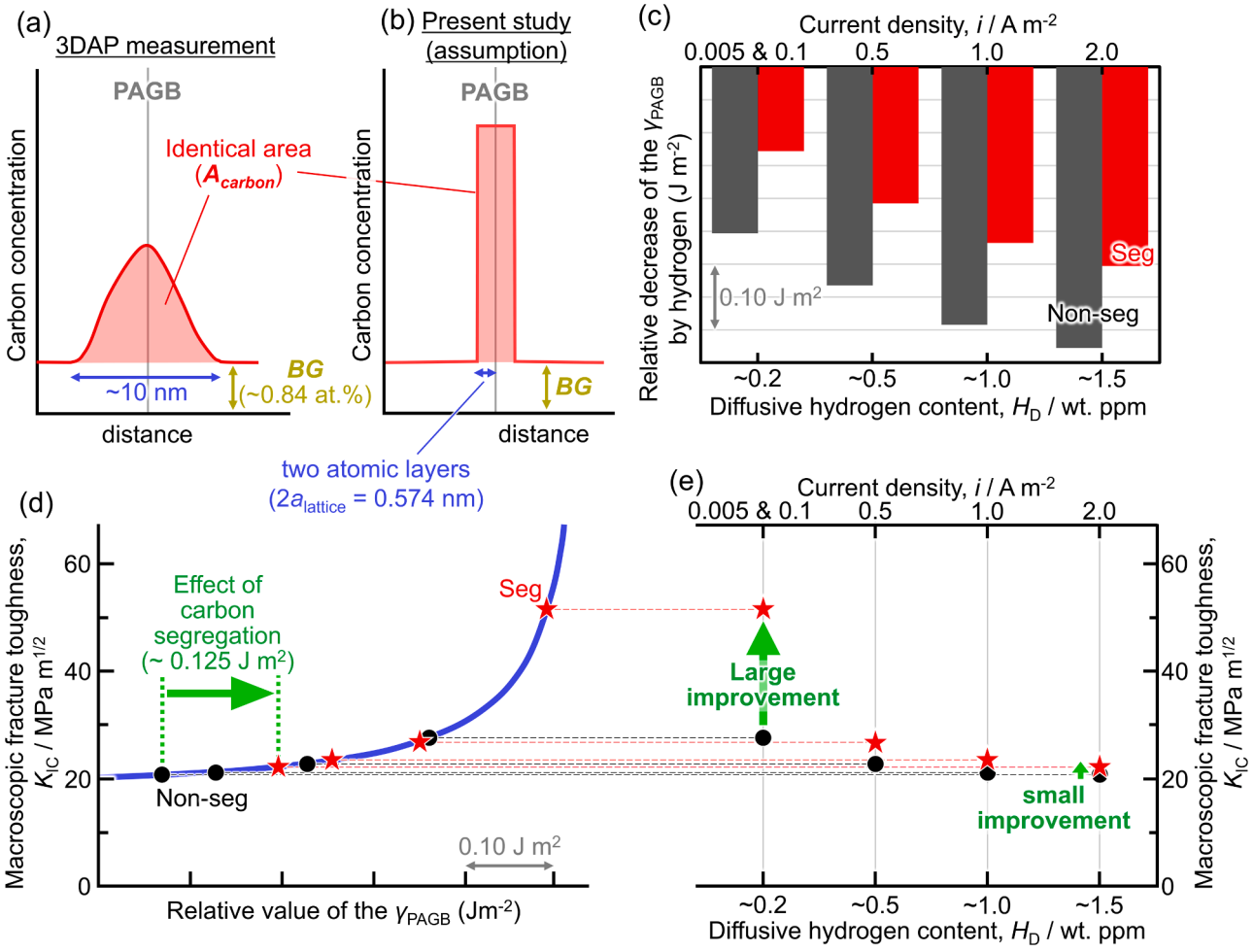


**Fig. 9.** (a, b) Schematic illustrations of carbon concentration profiles around PAGB (a) including the artifact of 3DAP measurement and (b) assuming that all of the segregated carbon atoms exist within the distance twice the lattice constant from PAGB. (c) Relative decreases of the $\gamma_{PAGB}$ by hydrogen in the Non-seg and Seg specimens. (d) The non-linear relationship between the $\gamma_{PAGB}$ and the $K_{IC}$ on which the relative values of the $\gamma_{PAGB}$ in the Non-seg and Seg specimens are plotted (the blue line in (d) was cited from [57]). (e) Relationship between the $K_{IC}$ obtained form (d) and the $H_D$.

**Table 1**
Concentrations of segregated carbon atoms at PAGB estimated directly from the 3DAP profiles [29] and those converted to the densities within the PAGB layer. Relative improvements of the $\gamma_{PAGB}$ in the Seg specimen against Non-seg specimen evaluated using the previous results of first-principles calculations [28].

| | Concentration of segregated carbon at PAGB | | Relative improvement of the $\gamma_{PAGB}$ in the Seg specimen ($\Delta\gamma_{PAGB}$) | | |
|---|---|---|---|---|---|
| | 3DAP [29] | Within PAGB layer ($X_{PAGB}$) | Immobile | Mobile | Intermediate value |
| Non-seg | 2.90 at.% | 13.53 at.% | 0.104 J $m^{-2}$ | 0.146 J $m^{-2}$ | 0.125 J $m^{-2}$ |
| Seg | 4.58 at.% | 18.73 at.% | | | |

reported that the segregation was within two atomic layers from GB. Therefore, in the present study, we evaluated the $X_{PAGB}$ based on the assumption that all the segregated carbon atoms exist within the distance twice the lattice constant ($2a_{lattice}$) from PAGB (0.574 nm, Fig. 9 (b)). The $X_{PAGB}$ were obtained by the following equation:

$$X_{PAGB} = BG + \frac{A_{carbon}}{4a_{lattice}} \quad (3)$$

where $BG$ is the background of the carbon concentration profile, approximately corresponding to the bulk average chemical composition of the present ingot (0.18 wt.%, 0.84 at.%). The $A_{carbon}$ is the integrated intensity of the profile with the $BG$ subtracted. The $X_{PAGB}$ was 13.53 at.% and 18.73 at.% in the Non-seg and Seg specimens, respectively (Table 1). According to the Hillert-Ohtani model [60,61], in which the local equilibrium between the GB layer and grain interior is considered, the $X_{PAGB}$ of ~15 at.% in the Fe-C [62] or Fe-Mn-C [63] system would be plausible. According to Yamaguchi et al. [28], when the hydrogen content in bulk lattice ($H_{lattice}$) is above $2 \times 10^{-4}$ wt. ppm ($10^{-8}$ atm. fract.) and the $X_{PAGB}$ is below 25 at.%, the $\gamma_{GB}$ of Σ3(111) iron GB increases by 0.20 J $m^{-2}$ ~ 0.28 J $m^{-2}$ for every 10 at.% increase in the $X_{PAGB}$. The increase of the $\gamma_{GB}$ ($\Delta\gamma_{GB\text{-}10\%}$) depends on the mobility of hydrogen at the moment of intergranular decohesion (immobile case: $\Delta\gamma_{GB\text{-}10\%} = 0.20$ J $m^{-2}$, mobile case: $\Delta\gamma_{GB\text{-}10\%} = 0.28$ J $m^{-2}$). Thus, the relative improvements of the $\gamma_{PAGB}$ in the Seg specimen against the Non-seg specimen ($\Delta\gamma_{PAGB}$) can be calculated by the following equation.

$$\Delta\gamma_{PAGB} = \Delta\gamma_{GB-10\%} \times [(18.73\,at.\% - 13.53\,at.\%)/10\,at.\%] \quad (4)$$

The $\Delta\gamma_{PAGB}$ is 0.104 J $m^{-2}$ for the immobile case and 0.146 J $m^{-2}$ for the mobile case (Table 1). In the present study, we used the $\Delta\gamma_{PAGB}$ as 0.125 J $m^{-2}$, which is the intermediate value between the immobile and mobile cases, because the detailed mobile effect of hydrogen on intergranular fracture has not been clarified. Yamaguchi et al. [28] also found that, when the $H_{lattice}$ doubles, the $\gamma_{GB}$ of Σ3(111) iron GB decreases by 0.06 J $m^{-2}$ at the $H_{lattice}$ above $2 \times 10^{-4}$ wt. ppm [24]. According to this relationship, the relative decreases of the $\gamma_{PAGB}$ by hydrogen in the Non-seg and Seg specimens were estimated as shown in Fig. 9(c), assuming that the $H_{lattice}$ is proportional to the $H_D$. In Fig. 9(d), the relative values of the $\gamma_{PAGB}$ are plotted on the non-linear relationship between the $\gamma_{PAGB}$ and the $K_{IC}$ (blue line) reported by Yamaguchi et al. [57]. We note that the relative values of the $\gamma_{PAGB}$ are determined but the absolute values of them and the corresponding $K_{IC}$ are provisional because we cannot know the absolute value of the local $H_{lattice}$ at the intergranular crack path. Thus, the following discussion is not completely quantitative but is semi-quantitative. In Fig. 9(e), the $K_{IC}$ obtained from (d) are plotted as a function of the $H_D$. At the low hydrogen content (below 0.2 wt. ppm), an increase in the $\gamma_{PAGB}$ significantly increases the $K_{IC}$, leading to the significant improvement of the fracture toughness properties in the Seg specimen. On the other hand, at the high hydrogen content (above 0.5 wt. ppm), the $K_{IC}$ is rather insensitive to the $\gamma_{PAGB}$, resulting in the minor improvement in the Seg specimens. The results semi-quantitatively demonstrate the consistency between the experimentally evaluated toughness properties ($J_{IC}$ and $T_R$) and the results of first-principles calculations ($\gamma_{GB}$, [28]) even at the high $H_D$. Here, we emphasize that the $\gamma_p$, which dominates the non-linear relationship between the $\gamma_{PAGB}$ and the toughness properties, is closely related with the plastic deformation associated with crack propagation, such as the local ductile fracture of small uncracked ligaments (Figs. 6 (a–c), 7(a–c), and 8) and the formation of dislocation cell structures / nano-voids within a lath (Figs. 6(d, e) and 7(d, e)).

We consider another factor that influences the relationship between the experimentally evaluated toughness properties ($J_{IC}$ and $T_R$) and the results of first-principles calculations ($\gamma_{GB}$). As shown in Figs. 6(a) and 7 (a), the degree of crack meandering was larger and the secondary crack length was longer in the Non-seg specimen than those in the Seg specimen at a current density of 0.005 A $m^{-2}$. To confirm this tendency at every test condition, both sides (upper and lower) of the fractured CT specimens were covered with resin, and the mid-thickness sections within 3 mm from the tip of fatigue pre-crack were observed using optical microscopy. Fig. 10 shows the optical microscopy images of one side of mid-thickness sections in the (a) uncharged Non-seg specimen, (b) hydrogen-charged Non-seg specimen (1.0 A $m^{-2}$), (e) uncharged Seg specimen, and (f) hydrogen-charged Seg specimen (1.0 A $m^{-2}$). Fig. 10 (c) is the enlarged view of the yellow dotted rectangle in (b). The fracture surfaces were macroscopically smooth and the secondary crack was rarely observed in the uncharged specimens (Fig. 10(a, e)). On the other hand, in the hydrogen-charged specimens (Fig. 10(b, c, f)), the fracture surfaces were rougher and the number of secondary cracks (indicated by the yellow arrows) was larger compared with those in the uncharged specimens. The values of the total observed crack length divided by the crack extension length ($L_{crack}/\Delta a$) in the Non-seg and Seg specimens are summarized as a function of $\Delta a$ in Fig. 10(d, g), respectively. The $L_{crack}$ was obtained using both the upper and lower fracture surface traces and the secondary cracks, while the $\Delta a$, evaluated according to ASTM E1820, is the projected crack length. In the uncharged specimens, the $L_{crack}$ was not much longer than $\Delta a$ ($L_{crack}/\Delta a \sim 1.2$) both in the Non-seg and Seg specimens. On the other hand, the $L_{crack}$ was much longer than $\Delta a$ in the hydrogen-charged specimens, particularly in the Non-seg specimens. The $L_{crack}/\Delta a$ value was approximately 3 in the Non-seg specimens, which was larger than that in the Seg specimens ($L_{crack}/\Delta a \sim 2$). This demonstrates that the total length of hydrogen-related crack ($L_{crack}$) is longer in the Non-seg specimens at an identical $\Delta a$. Therefore, we presume that the energy required for intergranular decohesion per unit area might be higher in the Seg specimens even though the total energy required for crack propagation per unit $\Delta a$ was almost the same between the Non-seg and Seg specimens at current densities above 0.5 A $m^{-2}$. However, when we precisely compare the hydrogen-related fracture toughness properties, the modified evaluation methods need to be established because almost all the fracture toughness test standards, such as ASTM E1820, do not consider the crack meandering and the existence of secondary cracks, i.e., they assume $L_{crack}/\Delta a \sim 1$. We believe that the effects of the crack meandering and the existence of secondary cracks on load – CMOD curve need to be clarified.

As explained above, we found that the effect of carbon segregation at PAGB on the fracture toughness properties depends on hydrogen concentration, i.e., carbon segregation effectively improved the $J_{IC}$ and $T_R$ at the low $H_D$ (below 0.2 wt. ppm) but is less effective at the high $H_D$ (above 0.5 wt. ppm). However, it was reported that the $H_D$ introduced under atmospheric corrosion is less than 0.2 wt. ppm in most of the high-strength steels [64–68]. Therefore, we can conclude that carbon segregation at PAGB is very effective in overcoming hydrogen embrittlement in the practical application of high-strength martensitic steels.

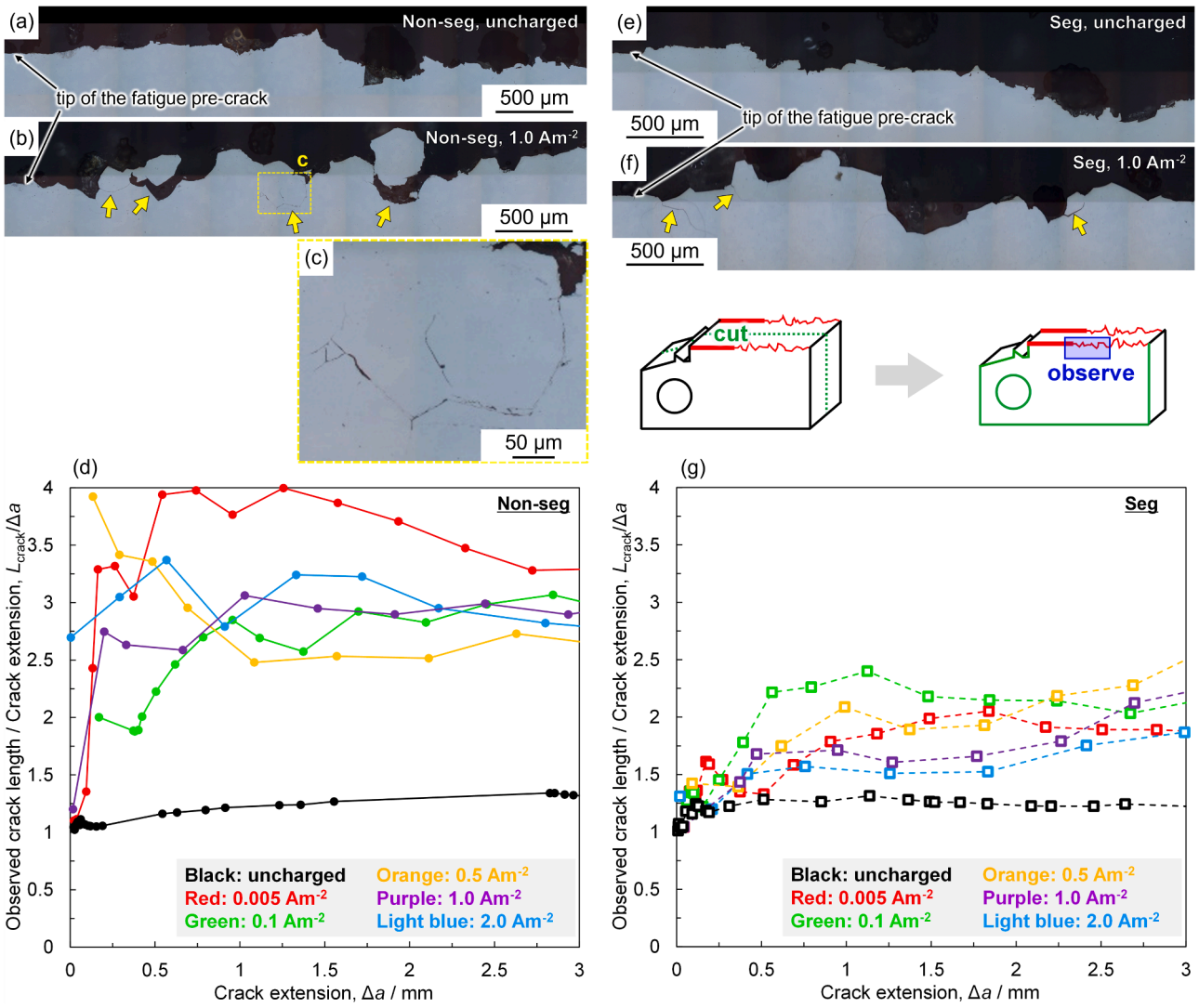


**Fig. 10.** Optical microscopy images of one side of mid-thickness sections in the fractured specimens after the unloading compliance tests ((a) uncharged Non-seg specimen, (b) hydrogen-charged Non-seg specimen (1.0 A $m^{-2}$), (e) uncharged Seg specimen, and (f) hydrogen-charged Seg specimen (1.0 A $m^{-2}$)). (c) is the enlarged view of the yellow dotted rectangle in (b). The yellow arrows indicate the positions of secondary cracks. (d, g) The values of the total observed crack length divided by the projected crack length ($L_{crack}/\Delta a$) against $\Delta a$ in the Non-seg and Seg specimens, respectively.

## 5. Conclusions

The present study quantitatively evaluated the effect of carbon segregation at PAGB on the fracture toughness properties under the presence of hydrogen and correlated them to the microscopic crack propagation behavior. The major conclusions are as follows:

1. The positive slopes of the $J - \Delta a$ resistance curves are confirmed after the start of crack propagation both in the Non-seg and Seg specimens, indicating that the hydrogen-related fracture is not a completely unstable brittle fracture, but involves a kind of stable crack propagation stage. The stable crack propagation is correlated with plastic deformation, such as the local ductile fracture of small uncracked ligaments and the formation of dislocation cell structures / nanovoids within a lath which lead to the hydrogen-related quasi-cleavage fracture.
2. At the low current densities below 0.1 A $m^{-2}$ ($H_D \sim 0.2$ wt. ppm), the fracture initiation toughness ($J_{IC}$) and tearing modulus ($T_R$), corresponding to crack growth resistance, were improved by carbon segregation. The improvement was attributed to the suppression of the accumulation of hydrogen around PAGB by site competition and the increase of PAGB cohesive energy.
3. At the high current densities above 0.5 A $m^{-2}$ ($H_D \geq 0.5$ wt. ppm), the $J_{IC}$ and $T_R$ did not change by carbon segregation. This result can appear to be not consistent with the previous results of first-principles calculations that the GB cohesive energy of iron was improved by carbon segregation even at the extremely high $H_D$ ($\sim 1.8 \times 10^3$ wt. ppm). However, considering the non-linear relationship between the toughness properties and the PAGB cohesive energy, the experimentally evaluated toughness properties ($J_{IC}$ and $T_R$) and the previously calculated GB cohesive energy were semi-quantitatively consistent even at the high hydrogen content.

## CRediT authorship contribution statement

**Kazuho Okada:** Writing – original draft, Resources, Methodology, Investigation, Funding acquisition, Formal analysis, Conceptualization. **Akinobu Shibata:** Writing – review & editing, Supervision, Resources, Project administration, Methodology, Funding acquisition, Conceptualization. **Yuuji Kimura:** Writing – review & editing, Resources, Formal analysis. **Masatake Yamaguchi:** Writing – review & editing, Validation,

Methodology, Conceptualization. **Ken-ichi Ebihara:** Writing – review & editing, Validation, Methodology, Conceptualization. **Nobuhiro Tsuji:** Writing – review & editing, Supervision, Resources, Funding acquisition, Conceptualization.

## Declaration of competing interest

The authors declare that they have no known competing financial interests or personal relationships that could have appeared to influence the work reported in this paper.

## Acknowledgments

This study was financially supported by JSPS KAKENHI (Nos. JP19J21267, JP20K21083, JP23K26410 and JP23K13541), Iketani Science and Technology Foundation (No. 0351190-A), and the Elements Strategy Initiative for Structural Materials (ESISM, No. JPMXP0112101000) through the Ministry of Education, Culture, Sports, Science and Technology (MEXT), Japan.

## Supplementary materials

Supplementary material associated with this article can be found, in the online version, at doi:10.1016/j.actamat.2024.120288.

## References

[1] S. Lynch, Hydrogen embrittlement phenomena and mechanisms, Corros. Rev. 30 (2012) 105–1023.
[2] I.M. Robertson, P. Sofronis, A. Nagao, M.L. Martin, S. Wang, D.W. Gross, K. E. Nygren, Hydrogen embrittlement understood, Metall. Mater. Trans. B 46 (2015) 1085–1103.
[3] M. Dadfarnia, A. Nagao, S. Wang, M.L. Martin, B.P. Somerday, P. Sofronis, Recent advances on hydrogen embrittlement of structural materials, Int. J. Fract. 196 (2015) 223–243.
[4] J. Venezuela, Q. Liu, M. Zhang, Q. Zhou, A. Atrens, A review of hydrogen embrittlement of martensitic advanced high-strength steels, Corros. Rev. 34 (2016) 153–186.
[5] M.L. Martin, M.J. Connolly, F.W. DelRio, A.J. Slifka, Hydrogen embrittlement in ferritic steels, Appl. Phys. Rev. 7 (2020) 041301.
[6] Y. Hagihara, T. Shobu, N. Hisamori, H. Suzuki, K. Takai, K. Hirai, Delayed fracture using CSRT and hydrogen trapping characteristics of V-bearing high-strength steel, ISIJ Int. 52 (2012) 298–306.
[7] A.R. Marder, G. Krauss, The morphology of martensite in iron-carbon alloys, Trans. Am. Soc. Met. 60 (1967) 651–660.
[8] G. Krauss, A.R. Marder, The morphology of martensite in iron alloys, Metall. Trans. 2 (1971) 2343–2357.
[9] S. Morito, H. Tanaka, R. Konishi, T. Furuhara, T. Maki, The morphology and crystallography of lath martensite in Fe-C alloys, Acta Mater. 51 (2003) 1789–1799.
[10] S. Morito, X. Huang, T. Furuhara, T. Maki, N. Hansen, The morphology and crystallography of lath martensite in alloy steels, Acta Mater. 54 (2006) 5323–5331.
[11] A. Shibata, G. Miyamoto, S. Morito, A. Nakamura, T. Moronaga, H. Kitano, I. G. Urrutia, T. Hara, K. Tsuzaki, Substructure and crystallography of lath martensite in as-quenched interstitial-free steel and low-carbon steel, Acta Mater. 246 (2023) 118675.
[12] M. Wang, E. Akiyama, K. Tsuzaki, Effect of hydrogen on the fracture behavior of high strength steel during slow strain rate test, Corros. Sci. 49 (2007) 4081–4097.
[13] A. Shibata, Y. Momotani, T. Murata, T. Matsuoka, M. Tsuboi, N. Tsuji, Microstructural and crystallographic features of hydrogen-related fracture in lath martensitic steels, Mater. Sci. Technol. 33 (2017) 1524–1532.
[14] A. Shibata, T. Murata, H. Takahashi, T. Matsuoka, N. Tsuji, Characterization of hydrogen-related fracture behavior in as-quenched low-carbon martensitic steel and tempered medium-carbon martensitic steel, Metall. Mater. Trans. A 46 (2015) 5685–5696.
[15] A. Shibata, I.G. Urrutia, A. Nakamura, K. Okada, G. Miyamoto, Y. Madi, J. Besson, T. Hara, K. Tsuzaki, Three-dimensional propagation behavior of hydrogen-related intergranular cracks in high-strength martensitic steel, Int. J. Hydrog. Energy 48 (2023) 34565–34574.
[16] S.J. Lee, J.A. Ronevich, G. Krauss, D.K. Matlock, Hydrogen Embrittlement of Hardened Low-carbon Sheet Steel, ISIJ Int. 50 (2010) 294–301.
[17] K. Takasawa, R. Ikeda, N. Ishikawa, R. Ishigaki, Effects of grain size and dislocation density on the susceptibility to high-pressure hydrogen environment embrittlement of high-strength low-alloy steels, Int. J. Hydrog. Energy 37 (2012) 2669–2675.
[18] R. Thodla, M.T.P. Paes, B. Gerst, Hydrogen assisted cracking of AISI 4137M steel in O&G environments, Int. J. Hydrog. Energy 40 (2015) 17051–17064.
[19] L.B. Peral, A. Zafra, J. Belzunce, C. Rodríguez, Effects of hydrogen on the fracture toughness of CrMo and CrMoV steels quenched and tempered at different temperatures, Int. J. Hydrog. Energy 44 (2019) 3953–3965.
[20] J. Ovejero-Garcia, Hydrogen microprint technique in the study of hydrogen in steels, J. Mater Sci. 20 (1985) 2623–2629.
[21] K. Takai, J. Seki, Y. Homma, Observation of trapping sites of hydrogen and deuterium in high-strength steels by using secondary ion mass spectrometry, Mater. Trans. 36 (1995) 1134–1139. JIM.
[22] Y. Momotani, A. Shibata, D. Terada, N. Tsuji, Effect of strain rate on hydrogen embrittlement in low-carbon martensitic steel, Int. J. Hydrog. Energy 42 (2017) 3371–3379.
[23] Y. Momotani, A. Shibata, T. Yonemura, Y. Bai, N. Tsuji, Effect of initial dislocation density on hydrogen accumulation behavior in martensitic steel, Scr. Mater. 178 (2020) 318–323.
[24] M. Yamaguchi, J. Kameda, K. Ebihara, Mobile effect of hydrogen on intergranular decohesion of iron: first-principles calculations, Philos. Mag. 92 (2012) 1349–1368. Corrigendum 92(2012), pp.3121-3124.
[25] S. Wang, M.L. Martin, I.M. Robertson, P. Sofronis, Effect of hydrogen environment on the separation of Fe grain boundaries, Acta Mater. 107 (2016) 279–288.
[26] M. Rajagopalan, M.A. Tschopp, K.N. Solanki, Grain boundary segregation of interstitial and substitutional impurity atoms in alpha-iron, JOM 66 (2014) 129–138.
[27] S.P. Jung, Y. Kwon, C.S. Lee, B.J. Lee, Influence of hydrogen on the grain boundary crack propagation in bcc iron: a molecular dynamics simulation, Comput. Mater. Sci. 149 (2018) 424–434.
[28] M. Yamaguchi, J. Kameda, Intergranular decohesion induced by mobile hydrogen in iron with and without segregated carbon: first-principles calculations, in: Proceedings of the International Hydrogen Conference (HIC 2012): Hydrogen-Materials Interactions, American Society of Mechanical Engineers (ASME) Press, 2014, pp. 747–755.
[29] K. Okada, A. Shibata, T. Sasaki, H. Matsumiya, K. Hono, N. Tsuji, Improvement of resistance against hydrogen embrittlement by controlling carbon segregation at prior austenite grain boundary in 3Mn-0.2C martensitic steels, Scr. Mater. 224 (2023) 115043.
[30] A. Shibata, Y. Madi, K. Okada, N. Tsuji, J. Besson, Mechanical and microstructural analysis on hydrogen-related fracture in a martensitic steel, Int. J. Hydrog. Energy 44 (2019) 29034–29046.
[31] L.B. Peral, A. Zafra, J. Belzunce, C. Rodríguez, Effects of hydrogen on the fracture toughness of CrMo and CrMoV steels quenched and tempered at different temperatures, Int. J. Hydrog. Energy 44 (2019) 3953–3965.
[32] R. Thodla, M.T.P. Paes, B. Gerst, Hydrogen assisted cracking of AISI 4137M steel in O&G environments, Int. J. Hydrog. Energy 40 (2015) 17051–17064.
[33] M. Nagumo, H. Yoshida, Y. Shimomura, T. Kadokura, Ductile crack growth resistance in hydrogen-charged steels, ISIJ Int. 42 (2001) 132–137.
[34] K.A. Nibur, B.P. Somerday, C.S. Marchi, J.W. Foulk III, M. Dadfarnia, P. Sofronis, The relationship between crack-tip strain and subcritical cracking thresholds for steels in high-pressure hydrogen gas, Metall. Mater. Trans. A 44 (2013) 248–269.
[35] B.P. Somerday, M. Dadfarnia, D.K. Balch, K.A. Nibur, C.H. Cadden, P. Sofronis, Hydrogen-assisted crack propagation in austenitic stainless steel fusion welds, Metall. Mater. Trans. A 40 (2009) 2350–2362.
[36] K.A. Nibur, B.P. Somerday, D.K. Balch, C.S. Marchi, The role of localized deformation in hydrogen-assisted crack propagation in 21Cr–6Ni–9Mn stainless steel, Acta Mater. 57 (2009) 3795–3809.
[37] K.A. Nibur, B.P. Somerday, D.K. Balch, C.S. Marchi, Effects of strength and microstructure on hydrogen-assisted crack propagation in 22Cr-13Ni-5Mn stainless steel forging, Metall. Mater. Trans. A 41 (2010) 3348–3357.
[38] H.F. Jackson, K.A. Nibur, C.S. Marchi, J.D. Puskar, B.P. Somerday, Hydrogen-assisted crack propagation in 304L/308L and 21Cr–6Ni–9Mn/308L austenitic stainless steel fusion welds, Corros. Sci. 60 (2012) 136–144.
[39] A. Shibata, I.G. Urrutia, K. Okada, G. Miyamoto, Y. Madi, J. Besson, K. Tsuzaki, Relationship between mechanical response and microscopic crack propagation behavior of hydrogen-related intergranular fracture in as-quenched martensitic steel, Mater. Sci. Eng. A 831 (2022) 142288.
[40] K.S. Chan, A new criterion for brittle-to-ductile fracture transition, Acta Metall. 37 (1989) 1217–1226.
[41] M. Tsuboi, A. Shibata, D. Terada, N. Tsuji, Role of different kinds of boundaries against cleavage crack propagation in low-temperature embrittlement of low-carbon martensitic steel, Metall. Mater. Trans. A 48 (2017) 3261–3268.
[42] A. Shibata, I.G. Urrutia, A. Nakamura, G. Miyamoto, Y. Madi, J. Besson, T. Hara, K. Tsuzaki, Multi-scale three-dimensional analysis on local arrestability of intergranular crack in high-strength martensitic steel, Acta Mater. 234 (2022) 118053.
[43] S. Lynch, Discussion of some recent literature on hydrogen-embrittlement mechanisms: addressing common misunderstandings, Corros. Rev. 37 (2019) 377–395.
[44] T. Neeraj, R. Srinivasan, J. Li, Hydrogen embrittlement of ferritic steels: observations on deformation microstructure, nanoscale dimples and failure by nano voiding, Acta Mater. 60 (2012) 5160–5171.
[45] K. Okada, A. Shibata, W. Gong, N. Tsuji, Effect of hydrogen on evolution of deformation microstructure in low-carbon steel with ferrite microstructure, Acta Mater. 225 (2022) 117549.
[46] K. Okada, A. Shibata, H. Matsumiya, N. Tsuji, Origin of serrated markings on the hydrogen-related quasi-cleavage fracture in low-carbon steel with ferrite microstructure, ISIJ Int. 62 (2022) 2081–2088.

[47] K. Okada, A. Shibata, N. Tsuji, Characteristics and formation mechanism of serrated markings on the hydrogen-related quasi-cleavage fracture in as quenched low-carbon martensitic steel, Scr. Mater. 234 (2023) 115568.
[48] T. Doshida, H. Suzuki, K. Takai, N. Oshima, T. Hirade, Enhanced lattice defect formation associated with hydrogen and hydrogen embrittlement under elastic stress of a tempered martensitic steel, ISIJ Int. 52 (2012) 198–207.
[49] H.K. Birnbaum, P. Sofronis, Hydrogen-enhanced localized plasticity—A mechanism for hydrogen-related fracture, Mater. Sci. Eng. A 176 (1994) 191–202.
[50] T. Tabata, H.K. Birnbaum, Direct observations of hydrogen enhanced crack propagation in iron, Scr. Metall. 18 (1984) 231–236.
[51] M. Nagumo, Function of hydrogen in embrittlement of high-strength steels, ISIJ Int. 41 (2001) 590–598.
[52] A.A. Griffith, The phenomena of rupture and flow in solids, Philos. Trans. R. Soc. A 221 (1921) 163–198.
[53] E. Orowan, Fracture and strength of solids, Rep. Prog. Phys. 12 (1949) 185–232.
[54] G.R. Irwin, Analysis of stresses and strains near the end of a crack traversing a plate, J. Appl. Mech. 24 (1957) 361–364.
[55] M.L. Jokl, V. Vitek, C.J. McMahon Jr., A microscopic theory of brittle fracture in deformable solids: a relation between ideal work to fracture and plastic work, Acta Metall. 28 (1980) 1479–1488.
[56] K. Higashida, M. Tanaka, A. Hartmaier, Y. Hoshino, Analyzing crack-tip dislocations and their shielding effect on fracture toughness, Mater. Sci. Eng. A 483-484 (2008) 13–18.
[57] M. Yamaguchi, J. Kameda, Multiscale thermodynamic analysis on fracture toughness loss induced by solute segregation in steel, Philos. Mag. 94 (2014) 2131–2149.
[58] M. Yamaguchi, K. Ebihara, M. Itakura, Multiscale thermodynamic analysis on hydrogen-induced intergranular cracking in an alloy steel with segregated solutes, Corros. Rev. 33 (2015) 547–557.
[59] M.P. Seah, Interface adsorption, embrittlement and fracture in metallurgy: a review, Surf. Sci. 53 (1975) 168–212.
[60] M. Hillert, “Lectures on the Theory of Phase Transformations”, ed. H.I. Aaronson, Metallurgical Society of AIME Press, (1975), p.36.
[61] H. Ohtani, M. Enoki, Thermodynamic study of grain boundary segregation, in: Proceedings of the 5th International Symposium on Steel Science, Tokyo, The Iron and Steel Institute of Japan, 2017, pp. 65–70.
[62] Y. Zhou, T. Masumura, T. Tsuchiyama, Verification of thermodynamic models for predicting grain boundary segregation of carbon and nitrogen in ferritic steels, ISIJ Int. 62 (2022) 278–280.
[63] T. Tokunaga, Y. Motomura, H. Era, T. Tsuchiyama, K. Shobu, M. Hasebe, H. Ohtani, Effect of alloying elements on grain boundary segregation of boron and carbon in α-Iron, Tetsu Hagané 109 (2023) 158–166.
[64] S. Toyoda, H. Kimura, M. Nagoshi, I. Kage, N. Yoshihara, J. Sakai, Effects of Cu addition on hydrogen absorption and diffusion properties of 1470 MPa grade thin-walled Steel tube under atmospheric corrosion, ISIJ Int. 41 (2011) 1516–1523.
[65] E. Akiyama, M. Wang, S. Li, Z. Zhang, Y. Kimura, N. Uno, K. Tsuzaki, Studies of evaluation of hydrogen embrittlement property of high-strength steels with consideration of the effect of atmospheric corrosion, Metall. Mater. Trans. A 44 (2013) 1290–1300.
[66] E. Akiyama, K. Matsukado, M. Wang, K. Tsuzaki, Evaluation of hydrogen entry into high strength steel under atmospheric corrosion, Corros. Sci. 52 (2010) 2758–2765.
[67] T. Kushida, Hydrogen entry into steel by atmospheric corrosion, ISIJ Int. 43 (2003) 470–474.
[68] E. Akiyama, S. Li, T. Shinohara, Z. Zhang, Kaneaki Tsuzaki, Hydrogen entry into Fe and high strength steels under simulated atmospheric corrosion, Electrochim. Acta 56 (2011) 1799–1805.